This article has been accepted for publication in a future issue of this journal, but has not been fully edited. Content may change prior to final publication. Citation information: DOI 10.1109/TMI.2020.3012932, IEEE Transactions on Medical Imaging

1

Amplified Flow Imaging (aFlow): A novel MRI-based tool to unravel the coupled dynamics between the human brain and cerebrovasculature

Javid Abderezaei, John Martinez, Itamar Terem, Gloria Fabris, Aymeric Pionteck, Yang Yang, Samantha J. Holdsworth, Kambiz Nael, and Mehmet Kurt

Abstract—With each heartbeat, periodic variations in arterial blood pressure are transmitted along the vasculature, resulting in localized deformations of the arterial wall and its surrounding tissue. Quantification of such motions may help understand various cerebrovascular conditions, yet it has proven technically challenging thus far. We introduce a new image processing algorithm called amplified Flow (aFlow) which allows to study the coupled brain-blood flow motion by combining the amplification of cine and 4D flow MRI. By incorporating a modal analysis technique known as dynamic mode decomposition into the algorithm, aFlow is able to capture the characteristics of transient events present in the brain and arterial wall deformation. Validating aFlow, we tested it on phantom simulations mimicking arterial walls motion and observed that aFlow displays almost twice higher SNR than its predecessor amplified MRI (aMRI). We then applied aFlow to 4D flow and cine MRI datasets of 5 healthy subjects, finding high correlations between blood flow velocity and tissue deformation in selected brain regions, with correlation values $r = 0.61, 0.59, 0.52$ for the pons, frontal and occipital lobe ($p < 0.001$). Finally, we explored the potential diagnostic applicability of aFlow by studying intracranial aneurysm dynamics, which seems to be indicative of rupture risk. In two patients, aFlow successfully visualized the imperceptible aneurysm wall motion, additionally quantifying the increase in the high frequency wall displacement after a one-year follow-up period ($20\%, 76\%$). These preliminary data suggest that aFlow may provide a novel imaging biomarker for the assessment of aneurysms evolution, with important potential diagnostic implications.

Javid Abderezaei, Gloria Fabris and Aymeric Pionteck are with the Department of Mechanical Engineering, Stevens Institute of Technology, Hoboken, NJ, 07030 USA.

John Martinez is with the Department of Biomedical Engineering, Stevens Institute of Technology, Hoboken, NJ, 07030 USA.

Itamar Terem is with the Department of Radiology, Stanford University, Stanford, CA, 94305 USA.

Yang Yang is with the Department of Radiology and BioMedical Engineering and Imaging Institute, Icahn School of Medicine at Mount Sinai, New York, NY 10029 USA.

Samantha J. Holdsworth is with the Department of Anatomy and Medical Imaging & Centre for Brain Research, Faculty of Medical and Health Sciences, University of Auckland, Auckland 1142 , New Zealand and also with Mātai Medical Research Institute, Gisborne-Tairāwhiti 4040 New Zealand.

Kambiz Nael is with the Department of Radiology, Icahn School of Medicine at Mount Sinai, New York, NY 10029 USA and also with the Department of Radiology, David Geffen School of medicine at UCLA, Los Angeles, CA 90095 USA.

Mehmet Kurt is with the with the Department of Mechanical Engineering, Stevens Institute of Technology, Hoboken, NJ, 07030 USA and also with the BioMedical Engineering and Imaging Institute, Icahn School of Medicine at Mount Sinai, New York, NY 10029 USA (e-mail: mkurt@stevens.edu).

Index Terms—Intracranial aneurysm, aneurysm rupture, 4D Flow MRI, cine MRI, amplified MRI.

I. Introduction

The human brain is not traditionally thought of as a mechanically active organ. Yet, due to its soft material properties and intricate boundary conditions (which include vasculature, cerebrospinal fluid (CSF), and dural folds [1]–[3]), it goes through constant motion and deformation states inside the skull. As the heart contracts and relaxes during the cardiac cycle, the periodic blood pressure variations that travel across the vasculature, deform the vessels along with the surrounding tissue [4]–[7]. Recent evidence suggests that brain dynamics and movement patterns might be altered in specific brain pathologies [8]–[11], which is why increasing interest is dedicated to understanding the coupled motion of the brain, CSF and blood flow [12]. In Chiari I malformation (CM-I), for instance, loss of proper CSF drainage into the spinal canal has been suggested to elevate the intracranial pressure, which in turn would alter the motion of the brain [13], [14]. Other pathologies that are thought to affect the drainage of CSF and alter motion include hydrocephalus and syringomyelia [9], [15], [16].

This coupled tissue-fluid motion has been previously investigated by various computational methods [17], [18]. For instance, Pahlavian *et al.* introduced a patient-specific, moving-boundary computational fluid dynamics (CFD) model of the cervical-medullary junction to study the central nervous system (CNS) tissue motion and its impact on the CSF dynamics [19]. Moireau *et al.* modeled the boundary condition between the vessel walls and the surrounding tissue as a viscoelastic support condition and suggested a framework to study the effect of blood flow on artery deformation, which in turn results in brain tissue movement [20].

Other studies evaluated these subtle motions through various imaging tools. By exploiting the velocity-encoding capability of phase-contrast MRI, for instance, the cardiac-induced motions in the brain, blood, and CSF flow can be tracked with high temporal resolution [21], [22]. Pujol *et al.* used this imaging technique to analyze CSF dynamics as well as the pulsatile motion of the brain in CM-I patients [8]. They reported obstruction of CSF flow from the cranial cavity to the spine in some patients as a result of abnormal motion of the cerebellar tonsils. Displacement encoded imaging with

stimulated echoes (DENSE) MRI is also a quantitative imaging tool that has been used in multiple studies to track the subtle motion of tissues [23]–[26]. This method has been shown to be able to detect brain motions as small as 0.04 mm [27]. Other imaging techniques such as cine balanced steady-state free precession (bSSFP) MRI (often referred to as cine MRI) has also been used to measure the cerebellar tonsil and hindbrain motion; however, with limited motion sensitivity, especially in the case of the human brain [9].

More recently, a new technique called amplified MRI (aMRI) was introduced [28]. Using aMRI, small motions that were difficult to track on cine MRI became more easily discernible through a Eulerian video magnification (EVM) algorithm [29]. aMRI was further improved by Terem *et al.* [30] by using a "phase-based" approach [31] which has better noise handling compared to its EVM predecessor. In such an aMRI approach, local phase variations corresponding to the motion are computed through complex steerable pyramids [32], and the evaluated temporal phase differences are then magnified with a specific amplification factor, enabling the visualization of imperceptible displacements through an advanced noise-filtering methodology. With this approach, the subtle motions of the brain were amplified, and abnormalities were found in the subsequent free form deformation maps of a CM-I patient [30]. In a nutshell, aMRI functions as a lens, magnifying the steady-state brain motion. But brain motion is intrinsically coupled to blood circulation, which is a prime example of a transient phenomenon, *i.e.* an event whose dynamical features change very rapidly [33] and that cannot be fully captured by aMRI.

Therefore, in this study, we further improved the aMRI method to extend its applicability also to the analysis of transient phenomena. This was mainly achieved through an incorporation of a modal analysis technique called dynamic mode decomposition (DMD) in aMRI's image processing pipeline [34]. Such modal analysis techniques have been previously used in studying the blood velocity profiles in human cardiovascular system [35]. Proper orthogonal decomposition (POD), for instance, was applied to 4D flow MRI data, resulting an improvement in error metrics, which in turn allowed for a more accurate computation of the flow velocity data [35]. Divergence-free wavelet transform is another technique that has been applied to 4D flow MRI and phantom data [36]. This method demonstrated an improvement in noise reduction, especially in the presence of discontinues and nondivergence-free components in the flow fields [36].

In the present work, through the incorporation of DMD in the aMRI's image processing algorithm, we enabled its applicability in capturing the transient phenomena. By adding the extra information on blood flow and tissue motion *coupling*, our novel technique (which we call *aFlow*), has the potential to be used in the analysis of a wide range of pathological conditions whose patterns of small motions are believed to be reflecting the general state of health of a tissue. This is especially important in the case of cerebral aneurysms, where blood circulation and wall motion are known to engage in a complex dynamical interplay, often causing difficult-to-predict wall thinning and potential rupture [37]. Aneurysm

rupture can have catastrophic consequences, with a mortality rate of up to 60% [38], and significant morbidity in about 50% of the survivors [39]. Therefore, reliable and quantifiable criteria enabling to monitor aneurysm progression and to predict rupture risk are critical in any clinical setting. Currently, however, there is no general consensus in the medical community as to what method can best deliver the most accurate indications of aneurysm's evolution, growth, and rupture risk. Typical parameters that are monitored, include the aneurysm size, location, multiplicity and shape [40], [41]. Among these risk factors, aneurysm size has been used as an objective quantifiable parameter in imaging models proposed to study the risks of aneurysm rupture, such as in the recently published PHASES score [42] and in the 2015 American Heart Association and American Stroke Association guideline management of unruptured aneurysms [43]. However, several studies have shown that aneurysm size alone is an imperfect measure for individualized risk stratification since a significant number of ruptured aneurysms can be small [44]–[46]. Recently, however, a number of studies have associated the risk of aneurysm rupture with changes in its wall motion [47]–[51]. Meyer *et al.*, for instance, used cine phase-contrast MRI to track the aneurysms' motion and observed that ruptured aneurysms had a larger variability in pulsatility compared to unruptured ones [52]. Using digital subtraction angiography, a correlation between abnormal aneurysm wall motion and a potential mechanism of injury such as wall shear stress (WSS) has been hypothesized [37]. 4D flow MRI which allows capturing dynamic, multi-directional blood velocity data is also one of the image acquisition methods that has been recently used to assess the aneurysm rupture risk [53], [54]. In short, in 4D flow MRI, the velocity is encoded in 3 spatial directions and a 3D velocity field is acquired [55]. Then, a post-processing algorithm is typically used to combine 3D velocity and magnitude data, allowing one to visualize the motion of the blood vessels. [56].

In order to extend the applicability of aMRI to the analysis of transient dynamics, in this work we further improved the aMRI image processing technique by introducing amplified Flow Imaging (aFlow). aFlow is a phase-based aMRI algorithm that uses DMD as a temporal filter and amplifies the sub-voxel motion of both the brain parenchyma and vasculature to enable better visualization of these motions. Using DMD in the algorithm, aFlow is able to retrieve the characteristics present in a transient event such as the vasculature motion [57], [58] observed in 4D flow MRI. The ability of aFlow to reveal sub-voxel motions was tested by using simple digital phantom simulations that mimic the pulsatile motion of arteries. Next, using aFlow data acquired on 5 healthy subjects, the correlation between the blood flow speed and the localized brain tissue deformation in regions surrounding the vasculature was analyzed. Finally, the potential diagnostic applicability of aFlow was tested by characterizing aneurysm wall motion. To do so, we applied aFlow to 4D flow MRI datasets acquired on two patients with intracranial aneurysm scans to evaluate how aneurysm wall motion changed over the course of one year.

II. METHODS

A. Human subjects

With institutional review board approval (IRB-17-01563) and informed consent, scans were performed on 5 healthy adult volunteers (3 females and 2 males between 48 and 63 years of age) to study the correlation between blood flow and the deformation of its surrounding tissue. Additionally, with IRB approval, an initial and a follow-up scan after 1 year were acquired on 2 aneurysm patients (Case 1: A 54 year old female and Case 2: A 32 year old male), in which, Case 1 aneurysm experienced a 1 mm increase in diameter after one year. Cross sections of the basilar arteries were chosen as the control and their deformation was compared with that of aneurysm walls.

B. Amplified Flow Imaging (aFlow) input data acquisition

Two imaging methods underlie the aFlow method: cine MRI, which is used to capture the movement of the brain parenchyma, and 4D flow MRI, which is used to capture the movement of the brains arterial vasculature. In both cases, a 3T whole-body GE MR750 Discovery MRI system (GE SIGNA scanner) and an 8-channel head coil were used to scan the patients. In the first step, cine MRI was used to obtain cardiac gated time-resolved data of each patient's brain. Cine MRI typically accomplishes this by using steady-state free procession (bSSFP) [59] and syncing the pulse sequence with the patient's heart rate through the use of an electrocardiogram or pulse oximeter. The process is repeated consistently to acquire all the spatial information needed to fill the k-space. Each frame or "cardiac phase" is tagged to a specific time in the cardiac cycle to create videos of the brain motion during one heartbeat [59]. For each subject, whole brain cine MRI were acquired using the following imaging parameters: acquisition matrix = 512×512, flip angle = $45°$, FOV = 180 mm, TR/TE = 3.66/1.18 ms, ±128 kHz bandwidth, 85 cardiac phases, and 14 slices with a thickness ranging from 4-5 mm.

Secondly, 4D flow MRI was used to track the motion of blood vessels [56]. This scan is based on traditional phase-contrast enhanced MRI, which determines the blood's velocity. Also acquired as a cine sequence, here the velocity was encoded in three directions to capture the blood flow for each cardiac phase. Before the visualization of the 4D flow MRI, the following de-noising steps were performed on the data-set: Phase-offset errors were corrected for Maxwell terms [60], gradient field nonlinearity [61] and eddy currents [62]. For the background phase errors, a second-order polynomial was fitted to the static regions of the image and subsequently subtracted from the velocity data [62]. Following these steps, the acquired magnitude data was combined with the 3D velocity information, allowing visualization of the blood vessels [56]. 4D flow MRI of the major cerebral arteries at the level of the circle of Willis were acquired based on the following imaging parameters: acquisition matrix = $224 \times 224 \times 75$, flip angle = $14°$, FOV = 180 mm, TR/TE = 5.76/3.1 ms, ±128 kHz bandwidth, 20 cardiac phases, temporal resolution of 40-60 ms (depending on the subject's heart rate), velocity encoding factor (VENC) = 3.5 cm/s and slice thickness of 1 mm.

C. aFlow algorithm

aFlow improves on the current aMRI technique [28], [30] by integrating a sophisticated modal analysis method into the algorithm which allows to precisely separate closely-spaced transient phenomena present in biological tissues; this technique is known as DMD [2], [63]. Specifically, in this work we apply aFlow to study the interplay between the blood and brain motion according to the following steps: First, appropriate cine MRI and 4D flow MRI datasets are selected as the input videos. Then, aFlow decomposes the local phases of each time frame at different scales and orientations using a linear complex-valued steerable pyramid ([31], see Fig. 1(a)). It should be noted that the variations between the acquired phases from the steerable pyramid correspond to displacements [31]. DMD is then incorporated in lieu of a temporal filter, allowing to isolate the motion in specific temporal frequencies and enabling analysis of highly transient phenomena. DMD achieves this by summing up the modes in the specified frequency range, which can be chosen based on the desired application. This modal analysis technique allows to capture the modal behavior of a data-set even in the absence of its governing model, and as such has found widespread applications in biomedical signal analysis, fluid and structural mechanics [64]–[66]. In order to use DMD, we constructed a displacement field $u(x, y, t)$ from the retrieved phase variations of the decomposed data (at each scale and orientation from the steerable pyramid) at different time points. Here, x and y are the spatial location of each node of the frame at time t. Assume that there are N equally spaced snapshots of M nodes, which in the case of video frames result in a 2 degrees of freedom at each snapshot. Using DMD, the displacement fields can be decomposed as follows:

$$u(x, y, t) = \sum_{n=1}^{N} a_n \exp(\lambda_n t) \phi_n(x, y) \qquad (1)$$

where $U_1^N = \{u_1, u_2, ..., u_N\}$. Here, a_n is the modal coefficient, λ_n is the complex modulus, and ϕ_n is the spatial distribution of each mode. DMD assumes a linear mapping between consecutive snapshots, where $u_{j+1} = Au_j$, that results in $U_1^N = \{u_1, Au_1, ..., A^{N-1}u_1\}$. The eigenvalues and eigenvectors of A are then evaluated using singular value decomposition (SVD) to form a companion matrix $\tilde{S} = H^T AH$, where H are the left singular vectors of U. By using the eigenvectors of $\tilde{S}$, the modes of the data can be represented as:

$$\Psi = U_1^{N-1}T \qquad (2)$$

where T_j are the left eigenvectors of $\tilde{S}$. It should be noted that the parameters λ_n are calculated through the eigenvalues of $\tilde{S}$ and the frequency ω_j corresponding to each mode is $\omega_j = \text{Re}(\lambda_n)$. In a nutshell, the aFlow uses DMD as a temporal filter by summing up the modes from the retrieved phases only in the specified frequency range, i.e., for a subset K of modes such that $K \leq N$. The displacement field is reconstructed as:

$$u_{Filtered}(x, y, t) \approx \sum_{m=1}^{K} a_m \exp(\lambda_m t) \phi_m(x, y) \qquad (3)$$

In the above equation, the m indexes correspond to K modes such that $\omega_{min} \leq \omega_j \leq \omega_{max}$ with $j = [1, K]$. For a more comprehensive description of the DMD method, see [34], [67], [68]. Having applied DMD on the retrieved phases in a specific temporal frequency range, an amplitude-weighted Gaussian spatial filter is then used to remove any unwanted noise that may later arise from the amplification. Next, the filtered phase components are multiplied by an amplification factor α and added back to the original phase data. Finally, the modified video is reconstructed by collapsing the steerable pyramid, resulting in an amplified video in the desirable range of frequencies [31]. The general pipeline of aFlow image processing algorithm is shown in Fig. 1.

D. Digital phantom simulations

Having developed the aFlow algorithm, it was tested on digital phantom models that mimic the motion of arteries during pulsatile flow in two steps (Fig. 2). In the first step, we validated the method and discerned the feasible amplification boundaries. In the second step, we proposed a modification to the phantom simulations and compared the image quality of aFlow output with respect to its predecessor aMRI.

Initially, a Gaussian filtered 2D thin-walled circular shell with radius r, thickness h, and constant pixel intensity of 1 was created in MATLAB (MathWorks, Natick, MA, version R2017b). This was followed by pixel intensity changes between 0 and 1 inside the circular phantom (Fig. 2(a)). In this simulation, the thin-walled shell represents the artery wall, while the interior pixel intensity changes imitate the blood flow inside the artery. The blood flow and the corresponding deformation of the arterial wall were simulated using the Womersley solution for thin-walled elastic circular shells which has often been used to study arterial deformation [69]–[71]. The equation of motion of the phantom at time t is [70]:

$$\frac{\partial^2 \eta}{\partial t^2} = \frac{p_\omega - p_0}{h\rho_\omega} - \frac{E}{(1-\nu^2)R\rho_\omega}\left(\frac{\eta}{R} + \nu\frac{\partial \xi}{\partial z}\right) \quad (4)$$

where $\text{Re}(\eta)$ and $\text{Re}(\xi)$ are the radial and axial displacements, respectively. Here, $\text{Re}(\cdot)$ denotes the real part of a scalar. p_0 represents the pressure on the outer and p_ω represents the pressure on the inner surface of the artery. R denotes the radius; h denotes the thickness and z denotes the axial position which is assumed a constant number in this study. Here, ρ_ω, E, and ν denote the density, Young's modulus, and Poisson ratio of the aneurysm wall, respectively. The axial u and radial v momentum equations as well as the continuity equation for an in-compressible Newtonian fluid representing the blood flow are as follows [70]:

$$\frac{\partial u}{\partial t} = -\frac{1}{\rho}\frac{\partial p}{\partial z} + \frac{\mu}{\rho}\left(\frac{\partial^2 u}{\partial r^2} + \frac{1}{r}\frac{\partial u}{\partial r}\right) \quad (5)$$

$$\frac{\partial v}{\partial t} = -\frac{1}{\rho}\frac{\partial p}{\partial r} + \frac{\mu}{\rho}\left(\frac{\partial^2 v}{\partial r^2} + \frac{1}{r}\frac{\partial v}{\partial r} - \frac{v}{r^2}\right) \quad (6)$$

$$\frac{\partial u}{\partial z} + \frac{\partial v}{\partial r} + \frac{v}{r} = 0 \quad (7)$$

with p, μ and ρ denoting the pressure, viscosity, and density of the fluid, respectively. Having constructed the fluid-structure

coupling based on Eq. 4 and Eq. 5-7, the radial displacement of the thin-walled shell is in the following form:

$$\eta(t) = Ce^{i\omega(t-z/c)} \quad (8)$$

where c is the wave propagation speed and C is a constant that is determined in [70]. For more information regarding the fluid-structure coupling at the interface of the circular shell and the utilized boundary conditions, see [70], [72].

TABLE I: Material and geometric properties of the phantom model mimicking arterial wall motion. Properties from [73]–[76] were used in the phantom simulations.

Phantom parameters	Assigned properties
R	1 mm
h	0.075 mm
ρ_ω	1366 kg/m^3
E	2.1 MPa
ν	0.45
μ	3.5×10^{-3} Pa.s
ρ	1060 kg/m^3

The simulated phantom model was then amplified using aFlow and converted into DICOM images with the same image matrix size as acquired *in vivo* (512×512).

In the first step, we investigated the dependence of amplified displacement on: varying amplification factor α between 0 and 7, varying internal pressure between 75 mmHg and 100 mmHg, and varying Rician noise parameter s between 0 and 0.01. A list of the material and geometric properties used in the digital phantom simulations (Eq. 4-7) can be found in Table I ([73]–[76]).

In the second step, we compared how sensitive aFlow and its predecessor aMRI are to noise. We incorporated a travelling wave motion - a common characteristic in vasculature dynamics [77], [78] - in the Womersley solution (Eq. 8) and calculated the temporal SNR for each of the methods. In this case, the radial displacement of the thin-walled shell is:

$$\eta(t, \theta) = C(e^{i\omega(n_1 t - z/c) + ik_1\theta} + e^{i\omega(n_2 t - z/c) + ik_2\theta}) \quad (9)$$

where n_1 and n_2 are the harmonic numbers, k_1 and k_2 are the wavelengths of each signal, and θ denotes the circular position along the thin-walled shell.
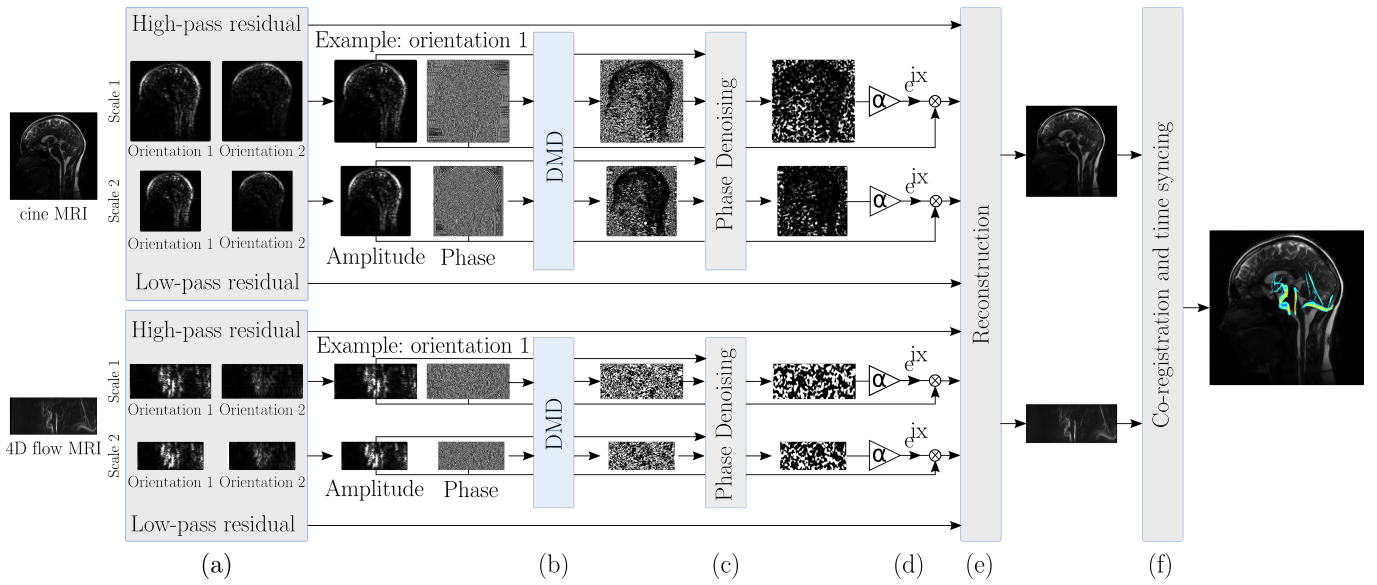
Fig. 1: **Schematics of the aFlow image processing technique**: aFlow decomposes the cine MRI and 4D flow MRI data in different scales and orientations and amplifies the local phases over time to visualize the subtle motion in the arteries and the brain. a) A linear complex-valued steerable pyramid is used on the cine MRI and 4D flow MRI input videos to decompose each time point into different spatial scales and orientations. These components are then separated into local phases and amplitudes. b) Dynamic mode decomposition (DMD) is used on each local phase to capture the transient characteristics of the cine MRI and 4D Flow data in the selected frequency range. c) The SNR of the captured phases is spatially improved using amplitude-weighted Gaussian spatial smoothing. d) The processed phases are amplified by the amplification factor and added to the original phase components. e) The amplified videos are reconstructed. f) The reconstructed cine MRI and 4D flow data are co-registered and the time of blood flow entering the brain and its following brain motion is synchronized.
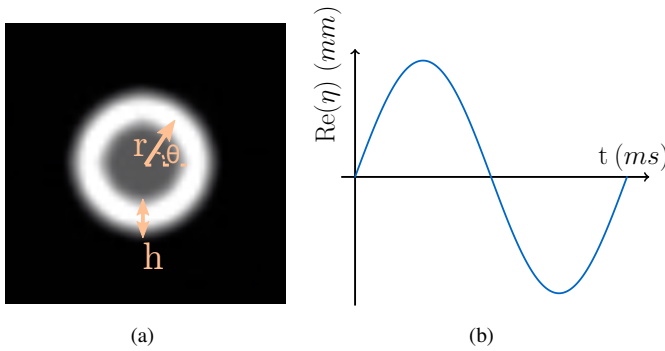

Fig. 2: **Simple digital phantom mimicking the pulsatile motion of an artery**. a) A phantom model mimicking the cross-section of an artery. b) A pulsatile motion based on the Womersley solution for thin-walled elastic circular shells is imposed on the phantom model. *$\mathrm{Re}(\cdot)$ denotes the real part of a scalar.

E. In vivo analysis

To check whether the acquired amplification boundaries in the digital phantom simulations lead to physiologically meaningful information, we tested aFlow on five healthy volunteers. Here, aFlow was used to individually amplify the acquired cine MRI and 4D flow MRI videos at $\alpha = 6$ and frequency range of $f = 0 - 1.7$ Hz. Next, to evaluate whether there is a correlation between the cerebrovascular deformation and the regional displacement of the brain, the acquired 4D Flow MRI data was registered to the cine MRI images. This allows proper alignment of the blood vessels in the brain tissue to evaluate the interplay between the blood flow and the brain motion. Here, ITK-SNAP (University of Pennsylvania, Philadelphia PA, and University of Utah, Salt Lake City, UT, version 3.6.0) was used to perform an initial manual rigid body transformation of the data. This was followed by an automated registration with ANTs (University of Pennsylvania, Philadelphia PA, [79]) to overlay the blood vessels in their corresponding areas in the cine MRI scans. The co-registration was then evaluated by an experienced radiologist. Finally, the Pearson's correlation coefficient r between the regional blood flow speed and the brain tissue's displacement r_U and the Lagrange strain r_E was calculated for the pons, frontal lobe, and occipital lobe and the results were averaged between 5 healthy subjects.

Next, we applied aFlow on two aneurysm patients. To visualize the motion in the major cerebral arteries, we chose $\alpha = 6$, and amplified 4D flow MRI videos of the two patients at the following frequency ranges: $f = 0 - 1.7$ Hz (denoted as "main harmonics") and $f > 1.7$ Hz (denoted as "higher frequencies"). $\alpha = 6$ was chosen since phantom simulations demonstrated a linear correlation between α and the amplified displacement for $\alpha \in [0, 7]$ (Fig. 3(a)). We have also found that the amplified displacement was still significantly correlated ($r > 0.96$, $p < 0.05$) with the ground truth for $\alpha \in [0, 10]$, regardless of the α of choice (Fig. 3(c)). The linear correlation between the amplified displacement

and α, however, was not present for $\alpha > 7$. As for the selected frequency band, since a resting heartbeat could reach a rate of approximately 1.7 Hz [80], we limited the main harmonics frequency range to this value. Additionally, nonlinear systems such as aneurysms are known to exhibit dynamics with super-harmonic resonances [78]. However, due to low time resolution of the acquired 4D flow MRI, the study of different harmonics (*e.g.* 2nd and 3rd) separately was not feasible. Here, because of that limitation, we assumed that the collective presence of the higher harmonics is the telltale sign of the nonlinear dynamics; hence, frequencies higher than 1.7 Hz were also amplified. After the amplification of the 4D flow data, an axial cross-section containing the aneurysm was selected. We then quantified the mean in-plane displacement of the aneurysm wall in the selected plane and compared it with the mean in-plane displacement of the basilar arteries (control group) in a selected axial cut.

F. Displacement tracking in the amplified videos

To quantitatively evaluate the displacement of the amplified videos, a free-form deformation algorithm developed in [81] was used to register each subsequent time frame (floating image) to the initial time frame (reference image). The floating image is locally deformed to match the reference using cubic B-Splines which guarantees continuous deformation [82]. The implemented algorithm uses normalized mutual information (NMI) to evaluate the similarity between the frames [82]. The NMI is a similarity measure based on the paired-intensity distribution. A larger level of information shared between the two images results in a higher NMI value. The optimization is based on a three levels pyramidal approach [81]. The final result is a displacement map that reflects the differences between the reference and the floating image. Using this algorithm, we were able to isolate the pixels of the wall of arteries and obtain their direction and amplitude of displacement.

III. RESULTS

A. Phantom simulations

For the phantom simulations based on the generated signal from Eq. 8, we observed a linear correlation between the amplified displacement and amplification factor for $\alpha \in [0, 7]$ ($R^2 \approx 0.94$, Fig. 3(a)). Similar results were observed as we varied the internal pressure of the phantom with a constant $\alpha = 6$, which again suggests a linear correlation between amplified displacement and true displacement ($R^2 \approx 0.87$, Fig. 3(b)). Additionally, the normalized mean displacement maps between the amplified displacement and the ground truth were compared (Fig. 3(c)). The high correlation value $r > 0.96$ between the amplified displacements and the ground truth, showed that upon increasing α, the pattern of motion does not change ($p < 0.05$, Fig. 3(c)). These results show that, within the aforementioned range of α and internal pressure, the amplified displacement is linearly correlated with the ground truth displacement (Fig. 3). This means that aFlow can visualize the subtle motions of the phantom model (not visible before amplification), while being independent from

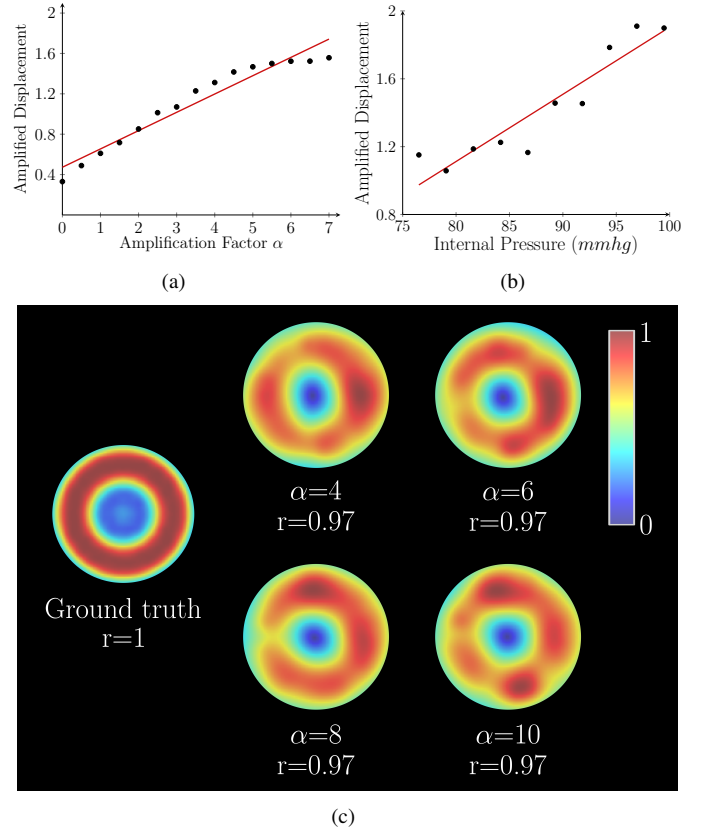parameters such as Rician noise, varying changes of intensity and partial volume effects (Fig. 3).

(a)   (b)

(c)

Fig. 3: Regression results between the amplified displacement and ground truth displacement for phantom models mimicking arterial pulsatility. A linear correlation was observed between the amplified displacement and a) The amplification factor α and b) The internal pressure. This suggests that, within this range of α and internal pressure, aFlow, amplifies the ground truth displacement linearly; thus, is independent from noise. c) Normalized mean of the phantom's displacement at different amplification factors was compared with the ground truth. This shows that with increasing the amplification factor the pattern of motion does not change.

After having incorporated travelling wave motion (Eq. 9) with two wavelength numbers (k_2, k_1) in the phantom model simulations, we amplified the videos using aFlow and aMRI. aFlow was found to be less sensitive to noise when compared to aMRI (Fig. 4). We observed that for a lower wavelength ratio of $k_2/k_1 = 1.25$, the SNR for aFlow and aMRI were similar (13.05 vs. 12.57, respectively (Fig. 4)). The SNR values for aFlow videos, however, was almost twice as high as the aMRI ones when k_2/k_1 was increased to 2.25 (13.04 vs. 6.01, respectively (Fig. 4)). This shows the capability of the incorporated DMD temporal filter in aFlow to more reliably capture the travelling wave characteristics when compared to the FFT-based temporal filter that is used in aMRI. In the limited case of a simple periodic loading (when $k_2/k_1 \approx 1$), DMD can be simplified to a Fourier analysis
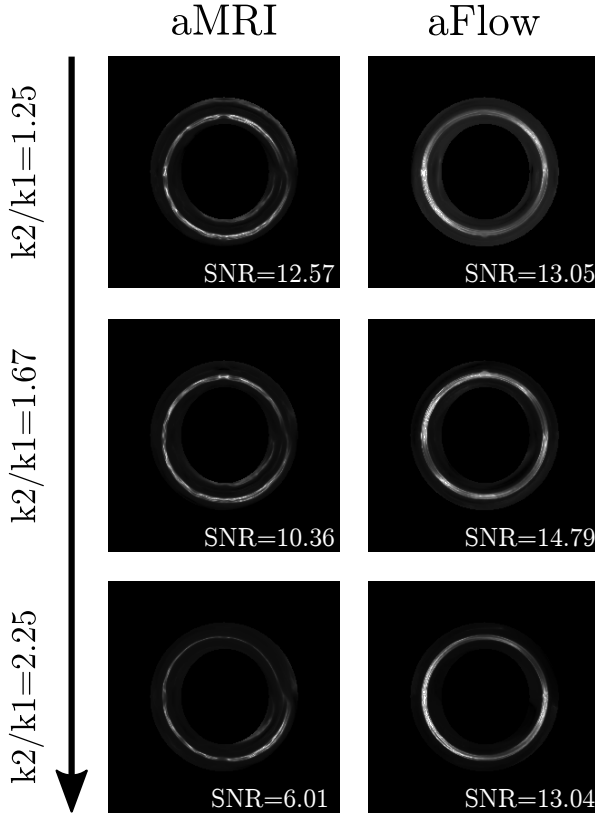
aMRI   aFlow

k2/k1=1.25

SNR=12.57   SNR=13.05

k2/k1=1.67

SNR=10.36   SNR=14.79

k2/k1=2.25

SNR=6.01   SNR=13.04

Fig. 4: Noise maps of aFlow and aMRI for phantom simulations with sub-voxel travelling wave motion in the phantom wall. As the wavelength ratio k_2/k_1 increased in the phantom models, the SNR for aFlow output videos experienced a negligible change, while for aMRI output videos it decreased by approximately 50%.

[83]. Here, however, since the input signal is in the form of a travelling wave, DMD seems advantageous for capturing the dynamics of the phantom motion.

B. In vivo validation

Before implementing aFlow as a tool to visualize the motion in the aneurysms, we analyzed whether it can capture the physiological coupling between the blood flow speed and the deformation of the brain. First, at each time-frame, the 3D velocity and magnitude data from 4D flow MRI was used to visualize the blood vessels. Next, we amplified the processed 4D flow MRI and cine MRI videos with $\alpha = 6$, since at this magnitude, the digital phantom simulations remained free of confounding noise (Fig. 3). After registration of the 4D flow MRI on the cine MR images (Fig. 5; see Supplemental Material, Video S1), we evaluated the correlation r between the deformation of the brain and blood flow speed at the pons, frontal lobe, and occipital lobe (Fig. 6). The average of the correlations between 5 healthy subjects is summarized in Table II. Here we observed r_U and r_E values of at least 0.52 and 0.51 across the aforementioned regions, respectively ($p < 0.001$; Table II). These results suggest that with the rush of blood flow into the major cerebral arteries, the brain tissue at
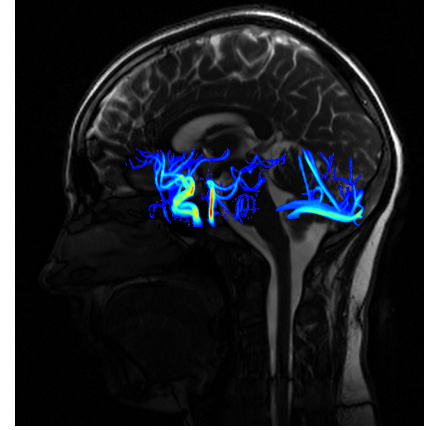

Fig. 5: Registration of the cerebral arteries on the brain.
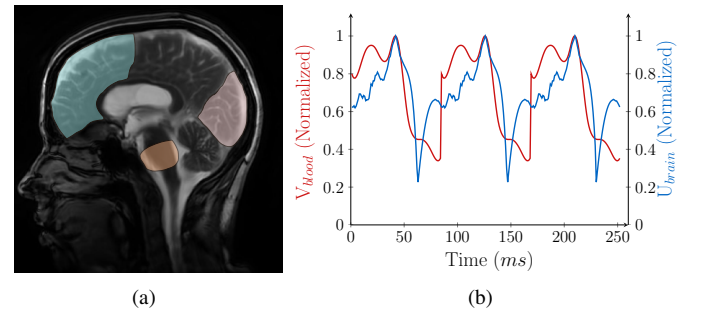

(a)   (b)

Fig. 6: Correlation between blood flow speed and deformation of the brain at specific regions. a) aFlow was utilized to visualize and evaluate the subtle motion in the arteries and the surrounding tissue in the pons, frontal, and occipital lobes for 5 healthy patients. b) Averaged blood flow speed (V_{blood}) and brain displacement (U_{brain}) in the occipital lobe for one subject. Note that blood speed and displacement curves were shifted to match their peak values.

those regions experience subtle deformation (see Supplemental Material, Video S1).

TABLE II: Averaged Pearson's correlation coefficients between averaged blood flow speed and brain tissue's displacement (r_U) or Lagrange strain (r_E) at different regions. For all of the cases $p < 0.001$.

Location	r_U	r_E
Pons	0.61 ± 0.18	0.69 ± 0.18
Frontal lobe	0.59 ± 0.09	0.51 ± 0.08
Occipital lobe	0.52 ± 0.08	0.51 ± 0.13

C. Application of aFlow in evaluating aneurysm wall motion

To test the potential ability of aFlow to analyze the biomechanics of a specific cerebrovascular condition, here we characterized the dynamics of the intracranial aneurysm wall in two patients who had a baseline scan and a follow up scan one year later. Case 1 was a 54 year old female with right internal carotid aneurysm which experienced a growth of approximately 1 mm over one year and was diagnosed

unstable. Case 2 was a 34 year old male with a basilar artery aneurysm which did not experience change in size over one year and was diagnosed stable. An $\alpha = 6$ was chosen since at this magnitude the digital phantom simulations remained free of confounding artifacts (Fig. 3). We observed that, while there was a negligible change in the basilar wall motion of both cases after one year, there was a substantial rise in the aneurysm wall displacement at higher frequencies (Fig. 7). Specifically, for both Case 1 and Case 2, the mean displacement of the basilar artery at the main harmonics and the higher frequencies decreased by less than 12% and 8% after one year, respectively (Fig. 7(a,c)). The mean displacement of aneurysm's wall at the main harmonics also experienced a negligible change of +4% and -1.5% in Case 1 and Case 2, respectively (Fig. 7(b,d)).

In Case 1, however, - a right internal carotid artery aneurysm characterized by interval growth - the mean displacement of the high frequency motion of the aneurysm wall showed a substantial increase of approximately 76% in the follow up motion when compared to the baseline scan (Fig. 7(b); see also Supplemental Material, Videos S2 and S3). Interestingly, because of its variation in size over the one year follow-up period, this patient's aneurysm was classified as unstable upon radiological examination. In Case 2 (a stable basilar artery aneurysm that did not change in size during the course of the follow-up), the mean displacement of aneurysm's wall at higher frequencies was only modestly increased (approximately 20%) when compared to the baseline scan (Fig. 7(d)).

IV. DISCUSSION

Movement is a ubiquitous feature of the living matter which ultimately affects physiological processes and organ function. Yet, the most subtle ways in which such motions unfold are often unexplored due to the lack of appropriate experimental methods and comprehensive analytical models to characterize tissue dynamics. At the same time, it is becoming clear that organ motion can be exploited as a marker describing the pathophysiological state of tissue; suffice to think of the widespread diagnostic use of techniques such as magnetic resonance elastography (MRE), which allows to assess tissue stiffness upon imaging the way shear waves propagate into the body [84]–[86].

To help fill this gap, in this paper we introduced a new image processing technique called aFlow that enables the frequency-selective amplification (hence, the visualization) of simultaneous soft tissue and vascular motion by post-processing standard clinical cine MRI and 4D flow imaging data, with potential application in the evaluation of various cerebrovascular disorders.

In the first step, we evaluated the feasible amplification boundaries of aFlow by testing various amplification factors on digital phantom models constructed to mimic the deformation of arteries during pulsatile flow. We observed that for the utilized parameters, aFlow successfully amplified the ground truth motion up to the amplification value of $\alpha = 7$, while retaining a linear dependence of the amplified displacement on the amplification factor. Additionally, while keeping α
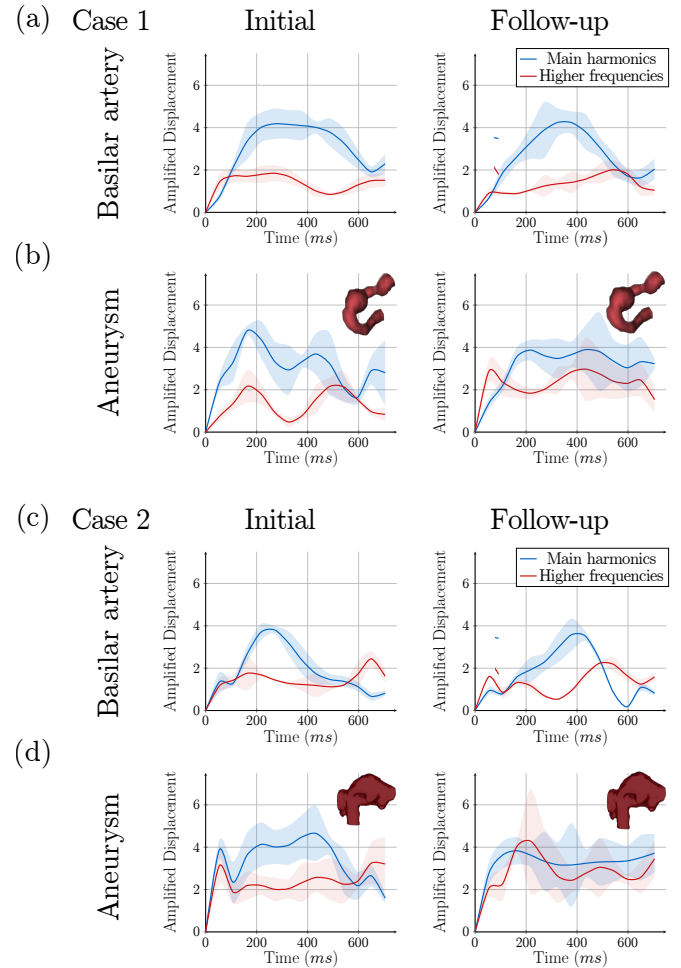

Fig. 7: **Amplified basilar and aneurysm wall deformation at two frequency ranges in two patients one year apart**: (a) In Case 1, the basilar artery does not experience a substantial change in its displacement at both frequency ranges. (b) The aneurysm's wall displacement at the main harmonics experiences a negligible change of +4%, while its motion at the higher frequencies varies by +76% after one year. (c) In Case 2, the basilar artery does not experience a substantial change in its displacement at both of the frequency ranges. (d) The aneurysm's wall displacement at the main harmonics experiences a negligible change of -1.5% for Case 2, while its motion at higher frequencies varies by +20% after one year. An outline of the aneurysms are shown for reference.

constant, we varied the boundary conditions of the simulations (by changing the internal arterial pressure in the model) and again found that the amplified displacement was independent of partial volume effect, Rician noise and varying phantom intensity.

The sensitivity of aFlow and its predecessor aMRI to noise was then calculated in the modified phantom models experiencing travelling wave motion as a combination of two input signals of different wavelength numbers (k_1 and k_2; see Eq. 9). We observed that with increasing wavelength number ratio k_2/k_1, the SNR for the aFlow amplified videos remained rather stable, whereas for the aMRI ones, it decreased by ap-

proximately 50%. This finding is in line with our expectations, given that DMD has been shown to have an advantage over FFT for transient systems [2], [63], as it provides a more accurate description of the system's response [63]. For the limited case of steady state motion in the phantom model, however, aFlow and aMRI showed comparable results. This highlights the potential ability of the DMD-based filter to capture the transient and non-stationary characteristics that exists in the motion of neurovasculature [78], [87], [88].

After the amplification boundaries of the algorithm were determined through the phantom models, we applied aFlow to *in vivo* cine MRI and 4D flow MRI data sets of 5 healthy subjects and analyzed whether the blood flow in the cerebral arteries could cause motion in the surrounding tissue. We calculated r_E and r_U correlation values in the range of approximately $0.50 - 0.60$ between the blood flow speed and the corresponding tissue deformation at the pons, frontal and occipital lobes ($p < 0.001$). This suggests a possible link between the blood flow, arterial deformation and the displacement of the brain tissue. Our findings are in agreement with [30], where by using aMRI, a high correlation was identified between the CSF/blood flow and the motion of mid-brain and pons. Similarly, these results are in line with previous work of Hirsch *et al.*, who applied motion-sensitive phase-contrast MRI and magnetic resonance elastography (MRE) to measure the volumetric strain of various brain structures, reporting that in the frontal and occipital lobes the latter would be related to the intracranial passage of the arterial pulse wave [12].

To demonstrate the potential application of this image processing technique to the characterization of a physiological disorder, we next applied aFlow to visualize aneurysm wall motion. This visualization is important since recent evidence has suggested that as aneurysms progress towards instability, their patterns of motion and deformation begin to change more erratically [37], [48]–[50]. A number of previous studies focused on analyzing the pulsatile patterns of unstable aneurysms [47], [89]: Ishida *et al.*, for instance, obtained 4-D CT movies and observed irregular pulsation in growing aneurysms in patients suffering from subarachnoid hemorrhage [47]. Neurosurgical assessment during endovascular intervention confirmed that these aneurysms had ruptured at sites of pulsating blebs [47]. Using the 4-D CT technique, it has also been found that the aneurysms' rupture point matched the location of observed wall motion during preoperative analysis in 2 out of 4 patients [89]. One of technical challenges reported by these studies, however, was the difficulty to accurately measure aneurysms' wall motion with conventional imaging techniques [90]; such deformations are in fact so small and often close to the imaging resolution, thereby rendering this approach ultimately unreliable in clinical settings [90]. Therefore, the capacity of aFlow to amplify and visualize sub-voxel motions makes it a promising candidate to be used in such studies.

The observed high frequency pulsatile motion of the intracranial aneurysms' wall could be due to several factors, such as its complex geometry and nonlinear material properties, as well as its interactions with the blood flow [78]. High-resolution, patient-specific computational fluid dynamics simulations have recently demonstrated the presence of "turbulent type" flow, characterized by transient high-frequency flow instabilities in some aneurysms [91]. Some studies revealed that such turbulent flows, associated with abnormal WSS, may lead to cell inflammation, and therefore may also be relevant for the assessment of intracranial aneurysms rupture risk [92], [93]. These simulations also demonstrated instability in the blood flow through high frequency fluctuations in pressure and velocity [94]. Such fluctuations of the blood flow could also result in a similar high frequency oscillations of the WSS in both magnitude and direction [94]. Consequently, capturing high-frequency arterial wall motion from aFlow could be an indicator of the presence of a turbulent regimen within the aneurysm, and therefore a possible indicator of risk of rupture.

In this work, aFlow successfully visualized and quantified aneurysm wall displacements from 4D flow data of two patients (Case 1 and Case 2) in which no motion was apparently discernible. In both cases, we observed that the basilar artery (control artery) experienced negligible changes in the one year follow-up studies. In the patient whose aneurysm demonstrated interval growth of $1\ mm$ in diameter (Case 1), we observed a substantial (76%) increase of the aneurysm wall motion at higher frequencies; for Case 2, this variation was of 20%. This difference might be due to the geometry and location of the aneurysms, more specifically to the fact that the second aneurysm was located at the top part of the basilar artery and in proximity of a branching point, where the blood flow input is divided into multiple outflows (Fig. 7(d)). This division could result in a decrease of the local blood flow velocity for Case 2. As a result, the aneurysm in Case 1 could be more exposed to locally elevated WSS, potentially translating into higher instability [95].

These findings demonstrate that aFlow is capable to visualize the hidden motions that exist in the human vasculature as acquired by 4D flow MRI and suggests, albeit in an extremely preliminary manner, a possible link between aneurysm instability and its motion at higher frequencies.

It is worth noting that, even though aFlow showed promising results in the phantom simulations, caution is advised when using this technique for *in vivo* analysis. The algorithm, in fact, works under the assumption that the motion in the studied problem is subtle and the variations of intensity not too substantial. If applied to visualize a motion that is already clearly visible, aFlow could introduce noise and artifacts to the input video. One limitation of this study is that out-of-plane motion is not detected, hence further work will be required to expand the aFlow algorithm to 3 dimensions in order to accurately amplify and evaluate motion in all spacial directions. To limit the effect of out-of-plane motion in the measured displacements, different planes containing the aneurysm were selected and amplified. For both of the aneurysm cases, an axial plane over the aneurysm, which showed the maximum displacement was selected for the comparisons in this study. Additionally, here we chose the amplification factor α based on phantom simulations specifically designed to mimic blood vessel pulsatility. We observed that by increasing α to 7, the displacement increased linearly and the pattern of motion remained the same as the ground truth. Upon increasing α further beyond this value, however, the simulations might give

rise to confounding artifacts. To use the proposed algorithm in other MRI domains, we recommend testing the input video with lower amplification factors in the beginning and then gradually increase α to find the optimum amplification value. Therefore, in order to evaluate the optimal algorithm's boundaries for application to other types of cardiovascular or neuroanatomical conditions, further work will be necessary.

Finally, we want to point out that our study does not attempt to draw conclusions on the definitive causal link between aneurysms' rupture risk and their high frequency motion; our sample size is obviously insufficient to answer such a complex, open, scientific question. However, the capability of aFlow to visualize amplified vascular wall motion will hopefully set a technical foundation, enabling future studies to investigate aneurysm dynamics more in depth, which might present profound clinical and diagnostic implications.

V. Conclusion

In this paper, we introduced aFlow, a novel image processing technique based on aMRI that allows more accurate visualization of sub-voxel tissue motion and better noise handling compared to its predecessor. With standard clinical cine MRI and 4D flow data as an input, aFlow allows for the amplification of subtle motions in the brain and the cerebrovasculature that would otherwise be difficult to measure. These subtle patterns of motion might hold important information regarding the physiological state of a tissue, as recently hypothesized for instance for the case of cerebral aneurysms. A preliminary analysis of 4D flow data from two patients highlighted the applicability of aFlow to analyzing the subtle pulsatile motion of intracranial aneurysms' walls. Given that aFlow is a post-processing algorithm carried out on a standard imaging technique, it holds great potential for being easily translated into the clinic. With further validation studies, aFlow could not only provide a unique imaging biomarker to complement the existing clinical and imaging tools for the follow-up of intracranial aneurysms, but might also be applied to a wide range of other clinical conditions such as hydrocephalus, Chiari malformation, and intracranial pressure abnormalities.

References

[1] J. Abderezaei, W. Zhao, C. L. Grijalva, G. Fabris, S. Ji, K. Laksari, and M. Kurt, "Nonlinear dynamical behavior of the deep white matter during head impact," *Physical Review Applied*, vol. 12, no. 1, p. 014058, 2019.

[2] K. Laksari, M. Kurt, H. Babaee, S. Kleiven, and D. Camarillo, "Mechanistic insights into human brain impact dynamics through modal analysis," *Physical Review Letters*, vol. 120, no. 13, p. 138101, 2018.

[3] A. Mojahed, J. Abderezaei, M. Kurt, L. A. Bergman, and A. F. Vakakis, "A nonlinear reduced-order model of the corpus callosum under planar coronal excitation," *Journal of Biomechanical Engineering*, vol. 142, no. 9, 2020.

[4] D. A. Feinberg and A. S. Mark, "Human brain motion and cerebrospinal fluid circulation demonstrated with MR velocity imaging," *Radiology*, vol. 163, no. 3, pp. 793–799, 1987.

[5] D. Chu, D. Levin, and N. Alperin, "Assessment of the biomechanical state of intracranial tissues by dynamic MRI of cerebrospinal fluid pulsations: a phantom study," *Magnetic Resonance Imaging*, vol. 16, no. 9, pp. 1043–1048, 1998.

[6] N. Alperin, E. M. Vikingstad, B. Gomez-Anson, and D. N. Levin, "Hemodynamically independent analysis of cerebrospinal fluid and brain motion observed with dynamic phase contrast MRI," *Magnetic Resonance in Medicine*, vol. 35, no. 5, pp. 741–754, 1996.

[7] M. E. Wagshul, P. K. Eide, and J. R. Madsen, "The pulsating brain: a review of experimental and clinical studies of intracranial pulsatility," *Fluids and Barriers of the CNS*, vol. 8, no. 1, p. 5, 2011.

[8] J. Pujol, C. Roig, A. Capdevila, A. Pou, J. Marti-Vilalta, J. Kulisevsky, A. Escartin, and G. Zannoli, "Motion of the cerebellar tonsils in chiari type i malformation studied by cine phase-contrast MRI," *Neurology*, vol. 45, no. 9, pp. 1746–1753, 1995.

[9] V. Leung, J. S. Magnussen, M. A. Stoodley, and L. E. Bilston, "Cerebellar and hindbrain motion in Chiari malformation with and without syringomyelia," *Journal of Neurosurgery: Spine*, vol. 24, no. 4, pp. 546–555, 2016.

[10] J. Weickenmeier, M. Kurt, E. Ozkaya, R. de Rooij, T. Ovaert, R. L. Ehman, K. B. Pauly, and E. Kuhl, "Brain stiffens post mortem," *Journal of the mechanical behavior of biomedical materials*, vol. 84, pp. 88–98, 2018.

[11] A. G. Chartrain, M. Kurt, A. Yao, R. Feng, K. Nael, J. Mocco, J. B. Bederson, P. Balchandani, and R. K. Shrivastava, "Utility of preoperative meningioma consistency measurement with magnetic resonance elastography (mre): a review," *Neurosurgical Review*, vol. 42, no. 1, pp. 1–7, 2019.

[12] S. Hirsch, D. Klatt, F. Freimann, M. Scheel, J. Braun, and I. Sack, "In vivo measurement of volumetric strain in the human brain induced by arterial pulsation and harmonic waves," *Magnetic Resonance in Medicine*, vol. 70, no. 3, pp. 671–683, 2013.

[13] E. Hofmann, M. Warmuth-Metz, M. Bendszus, and L. Solymosi, "Phase-contrast MR imaging of the cervical CSF and spinal cord: Volumetric motion analysis in patients with Chiari I malformation," *American Journal of Neuroradiology*, vol. 21, no. 1, pp. 151–158, 2000.

[14] N. Alperin, J. R. Loftus, C. J. Oliu, A. M. Bagci, S. H. Lee, B. Ertl-Wagner, B. Green, and R. Sekula, "Magnetic resonance imaging measures of posterior cranial fossa morphology and cerebrospinal fluid physiology in Chiari malformation type I," *Neurosurgery*, vol. 75, no. 5, pp. 515–522, 2014.

[15] O. Balédent, C. Gondry-Jouet, M.-E. Meyer, G. De Marco, D. Le Gars, M.-C. Henry-Feugeas, and I. Idy-Peretti, "Relationship between cerebrospinal fluid and blood dynamics in healthy volunteers and patients with communicating hydrocephalus," *Investigative Radiology*, vol. 39, no. 1, pp. 45–55, 2004.

[16] D. Enzmann and N. Pelc, "Normal flow patterns of intracranial and spinal cerebrospinal fluid defined with phase-contrast cine mr imaging," *Radiology*, vol. 178, no. 2, pp. 467–474, 1991.

[17] A. A. Linninger, M. Xenos, B. Sweetman, S. Ponkshe, X. Guo, and R. Penn, "A mathematical model of blood, cerebrospinal fluid and brain dynamics," *Journal of mathematical biology*, vol. 59, no. 6, pp. 729–759, 2009.

[18] B. J. Misgeld, R. Mondal, and S. Leonhardt, "Pulsatile cerebrospinal model with cardio-vascular coupling," *IFAC-PapersOnLine*, vol. 48, no. 20, pp. 183–188, 2015.

[19] S. H. Pahlavian, F. Loth, M. Luciano, J. Oshinski, and B. A. Martin, "Neural tissue motion impacts cerebrospinal fluid dynamics at the cervical medullary junction: A patient-specific moving-boundary computational model," *Annals of Biomedical Engineering*, vol. 43, no. 12, pp. 2911–2923, 2015.

[20] P. Moireau, N. Xiao, M. Astorino, C. A. Figueroa, D. Chapelle, C. Taylor, and J.-F. Gerbeau, "External tissue support and fluid–structure simulation in blood flows," *Biomechanics and Modeling in Mechanobiology*, vol. 11, no. 1-2, pp. 1–18, 2012.

[21] J. S. Tsuruda, A. Shimakawa, N. J. Pelc, and D. Saloner, "Dural sinus occlusion: evaluation with phase-sensitive gradient-echo MR imaging," *American Journal of Neuroradiology*, vol. 12, no. 3, pp. 481–488, 1991.

[22] D. Enzmann and N. Pelc, "Brain motion: measurement with phase-contrast mr imaging," *Radiology*, vol. 185, no. 3, pp. 653–660, 1992.

[23] A. H. Aletras, S. Ding, R. S. Balaban, and H. Wen, "DENSE: displacement encoding with stimulated echoes in cardiac functional MRI," *Journal of Magnetic Resonance*, vol. 137, no. 1, p. 247, 1999.

[24] X. Zhong, P. A. Helm, and F. H. Epstein, "Balanced multipoint displacement encoding for DENSE MRI," *Magnetic Resonance in Medicine: An Official Journal of the International Society for Magnetic Resonance in Medicine*, vol. 61, no. 4, pp. 981–988, 2009.

[25] A. H. Aletras, R. S. Balaban, and H. Wen, "High-resolution strain analysis of the human heart with fast-DENSE," *Journal of Magnetic Resonance*, vol. 140, no. 1, pp. 41–57, 1999.

[26] B. S. Spottiswoode, X. Zhong, C. H. Lorenz, B. M. Mayosi, E. M. Meintjes, and F. H. Epstein, "Motion-guided segmentation for cine DENSE MRI," *Medical Image Analysis*, vol. 13, no. 1, pp. 105–115, 2009.

This article has been accepted for publication in a future issue of this journal, but has not been fully edited. Content may change prior to final publication. Citation information: DOI 10.1109/TMI.2020.3012932, IEEE Transactions on Medical Imaging

11

[27] X. Zhong, C. H. Meyer, D. J. Schlesinger, J. P. Sheehan, F. H. Epstein, J. M. Larner, S. H. Benedict, P. W. Read, K. Sheng, and J. Cai, "Tracking brain motion during the cardiac cycle using spiral cine-DENSE MRI," *Medical Physics*, vol. 36, no. 8, pp. 3413–3419, 2009.

[28] S. J. Holdsworth, M. S. Rahimi, W. W. Ni, G. Zaharchuk, and M. E. Moseley, "Amplified magnetic resonance imaging (aMRI)," *Magnetic Resonance in Medicine*, vol. 75, no. 6, pp. 2245–2254, 2016.

[29] H.-Y. Wu, M. Rubinstein, E. Shih, J. Guttag, F. Durand, and W. Freeman, "Eulerian video magnification for revealing subtle changes in the world," 2012.

[30] I. Terem, W. W. Ni, M. Goubran, M. S. Rahimi, G. Zaharchuk, K. W. Yeom, M. E. Moseley, M. Kurt, and S. J. Holdsworth, "Revealing subvoxel motions of brain tissue using phase-based amplified MRI (aMRI)," *Magnetic Resonance in Medicine*, 2018.

[31] N. Wadhwa, M. Rubinstein, F. Durand, and W. T. Freeman, "Phase-based video motion processing," *ACM Transactions on Graphics (TOG)*, vol. 32, no. 4, p. 80, 2013.

[32] E. P. Simoncelli and W. T. Freeman, "The steerable pyramid: A flexible architecture for multi-scale derivative computation," in *Proceedings, International Conference on Image Processing*, vol. 3. IEEE, 1995, pp. 444–447.

[33] B. M. Johnston, P. R. Johnston, S. Corney, and D. Kilpatrick, "Non-newtonian blood flow in human right coronary arteries: transient simulations," *Journal of biomechanics*, vol. 39, no. 6, pp. 1116–1128, 2006.

[34] P. J. Schmid, "Dynamic mode decomposition of numerical and experimental data," *Journal of Fluid Mechanics*, vol. 656, pp. 5–28, 2010.

[35] M. F. Fathi, A. Bakhshinejad, A. Baghaie, D. Saloner, R. H. Sacho, V. L. Rayz, and R. M. DSouza, "Denoising and spatial resolution enhancement of 4d flow mri using proper orthogonal decomposition and lasso regularization," *Computerized Medical Imaging and Graphics*, vol. 70, pp. 165–172, 2018.

[36] F. Ong, M. Uecker, U. Tariq, A. Hsiao, M. T. Alley, S. S. Vasanawala, and M. Lustig, "Robust 4d flow denoising using divergence-free wavelet transform," *Magnetic resonance in medicine*, vol. 73, no. 2, pp. 828–842, 2015.

[37] E. Oubel, M. De Craene, C. M. Putman, J. R. Cebral, and A. F. Frangi, "Analysis of intracranial aneurysm wall motion and its effects on hemodynamic patterns," in *Medical Imaging 2007: Physiology, Function, and Structure from Medical Images*, vol. 6511. International Society for Optics and Photonics, 2007, p. 65112A.

[38] G. J. Rinkel, M. Djibuti, A. Algra, and J. Van Gijn, "Prevalence and risk of rupture of intracranial aneurysms: a systematic review," *Stroke*, vol. 29, no. 1, pp. 251–256, 1998.

[39] E. S. Connolly Jr, A. A. Rabinstein, J. R. Carhuapoma, C. P. Derdeyn, J. Dion, R. T. Higashida, B. L. Hoh, C. J. Kirkness, A. M. Naidech, C. S. Ogilvy *et al.*, "Guidelines for the management of aneurysmal subarachnoid hemorrhage: a guideline for healthcare professionals from the american heart association/american stroke association," *Stroke*, vol. 43, no. 6, pp. 1711–1737, 2012.

[40] N. Etminan, K. Beseoglu, D. L. Barrow, J. Bederson, R. D. Brown Jr, E. S. Connolly Jr, C. P. Derdeyn, D. Hänggi, D. Hasan, S. Juvela *et al.*, "Multidisciplinary consensus on assessment of unruptured intracranial aneurysms: proposal of an international research group," *Stroke*, vol. 45, no. 5, pp. 1523–1530, 2014.

[41] W. Brinjikji, Y.-Q. Zhu, G. Lanzino, H. Cloft, M. H. Murad, Z. Wang, and D. F. Kallmes, "Risk factors for growth of intracranial aneurysms: A systematic review and meta-analysis," *American Journal of Neuroradiology*, vol. 37, no. 4, pp. 615–620, 2016.

[42] J. P. Greving, M. J. Wermer, R. D. Brown Jr, A. Morita, S. Juvela, M. Yonekura, T. Ishibashi, J. C. Torner, T. Nakayama, G. J. Rinkel *et al.*, "Development of the PHASES score for prediction of risk of rupture of intracranial aneurysms: a pooled analysis of six prospective cohort studies," *The Lancet Neurology*, vol. 13, no. 1, pp. 59–66, 2014.

[43] B. G. Thompson, R. D. Brown Jr, S. Amin-Hanjani, J. P. Broderick, K. M. Cockroft, E. S. Connolly Jr, G. R. Duckwiler, C. C. Harris, V. J. Howard, S. C. Johnston *et al.*, "Guidelines for the management of patients with unruptured intracranial aneurysms: a guideline for healthcare professionals from the american heart association/american stroke association," *Stroke*, vol. 46, no. 8, pp. 2368–2400, 2015.

[44] M. Korja, R. Kivisaari, B. R. Jahromi, and H. Lehto, "Size and location of ruptured intracranial aneurysms: Consecutive series of 1993 hospital-admitted patients," *Journal of Neurosurgery*, vol. 127, no. 4, pp. 748–753, 2017.

[45] Y. Ohashi, T. Horikoshi, M. Sugita, T. Yagishita, and H. Nukui, "Size of cerebral aneurysms and related factors in patients with subarachnoid hemorrhage," *Surgical Neurology*, vol. 61, no. 3, pp. 239–245, 2004.

[46] T. R. Forget Jr, R. Benitez, E. Veznedaroglu, A. Sharan, W. Mitchell, M. Silva, and R. H. Rosenwasser, "A review of size and location of ruptured intracranial aneurysms," *Neurosurgery*, vol. 49, no. 6, pp. 1322–1326, 2001.

[47] F. Ishida, H. Ogawa, T. Simizu, T. Kojima, and W. Taki, "Visualizing the dynamics of cerebral aneurysms with four-dimensional computed tomography angiography," *Neurosurgery*, vol. 57, no. 3, pp. 460–471, 2005.

[48] C. Karmonik, O. Diaz, R. Grossman, and R. Klucznik, "In-vivo quantification of wall motion in cerebral aneurysms from 2D cine phase contrast magnetic resonance images," in *RöFo-Fortschritte auf dem Gebiet der Röntgenstrahlen und der bildgebenden Verfahren*, vol. 182, no. 02. © Georg Thieme Verlag KG Stuttgart· New York, 2010, pp. 140–150.

[49] D. Hadizadeh, C. Marx, J. Gieseke, H. Schild, and W. Willinek, "High temporal and high spatial resolution mr angiography (4D-MRA)," in *RöFo-Fortschritte auf dem Gebiet der Röntgenstrahlen und der bildgebenden Verfahren*, vol. 186, no. 09. © Georg Thieme Verlag KG, 2014, pp. 847–859.

[50] A. Vanrossomme, O. F. Eker, J.-P. Thiran, G. Courbebaisse, and K. Z. Boudjeltia, "Intracranial aneurysms: Wall motion analysis for prediction of rupture," *American Journal of Neuroradiology*, vol. 36, no. 10, pp. 1796–1802, 2015.

[51] R. Kleinloog, J. Zwanenburg, B. Schermers, E. Krikken, Y. Ruigrok, P. Luijten, F. Visser, L. Regli, G. Rinkel, and B. Verweij, "Quantification of intracranial aneurysm volume pulsation with 7T MRI," *American Journal of Neuroradiology*, vol. 39, no. 4, pp. 713–719, 2018.

[52] F. B. Meyer, J. Huston, and S. S. Riederer, "Pulsatile increases in aneurysm size determined by cine phase-contrast mr angiography," *Journal of neurosurgery*, vol. 78, no. 6, pp. 879–883, 1993.

[53] T. A. Hope, M. D. Hope, D. D. Purcell, C. von Morze, D. B. Vigneron, M. T. Alley, and W. P. Dillon, "Evaluation of intracranial stenoses and aneurysms with accelerated 4d flow," *Magnetic resonance imaging*, vol. 28, no. 1, pp. 41–46, 2010.

[54] S. Schnell, C. Wu, and S. A. Ansari, "4d mri flow examinations in cerebral and extracerebral vessels. ready for clinical routine?" *Current opinion in neurology*, vol. 29, no. 4, p. 419, 2016.

[55] Z. Stankovic, B. D. Allen, J. Garcia, K. B. Jarvis, and M. Markl, "4d flow imaging with mri," *Cardiovascular diagnosis and therapy*, vol. 4, no. 2, p. 173, 2014.

[56] M. Markl, A. Frydrychowicz, S. Kozerke, M. Hope, and O. Wieben, "4D flow MRI," *Journal of Magnetic Resonance Imaging*, vol. 36, no. 5, pp. 1015–1036, 2012.

[57] H. Baek, M. Jayaraman, P. Richardson, and G. Karniadakis, "Flow instability and wall shear stress variation in intracranial aneurysms," *Journal of the Royal Society Interface*, vol. 7, no. 47, pp. 967–988, 2009.

[58] L. Grinberg, A. Yakhot, and G. E. Karniadakis, "Analyzing transient turbulence in a stenosed carotid artery by proper orthogonal decomposition," *Annals of Biomedical Engineering*, vol. 37, no. 11, pp. 2200–2217, 2009.

[59] A. Oppelt, R. Graumann, H. Barfuss, H. Fischer, W. Hartl, W. Schajor *et al.*, "Fispa new fast mri sequence," *Electromedica*, vol. 54, no. 1, pp. 15–18, 1986.

[60] M. A. Bernstein, X. J. Zhou, J. A. Polzin, K. F. King, A. Ganin, N. J. Pelc, and G. H. Glover, "Concomitant gradient terms in phase contrast mr: analysis and correction," *Magnetic resonance in medicine*, vol. 39, no. 2, pp. 300–308, 1998.

[61] M. Markl, R. Bammer, M. Alley, C. Elkins, M. Draney, A. Barnett, M. Moseley, G. Glover, and N. Pelc, "Generalized reconstruction of phase contrast mri: analysis and correction of the effect of gradient field distortions," *Magnetic Resonance in Medicine: An Official Journal of the International Society for Magnetic Resonance in Medicine*, vol. 50, no. 4, pp. 791–801, 2003.

[62] P. G. Walker, G. B. Cranney, M. B. Scheidegger, G. Waseleski, G. M. Pohost, and A. P. Yoganathan, "Semiautomated method for noise reduction and background phase error correction in mr phase velocity data," *Journal of Magnetic Resonance Imaging*, vol. 3, no. 3, pp. 521–530, 1993.

[63] C. W. Rowley, I. Mezić, S. Bagheri, P. Schlatter, and D. S. Henningson, "Spectral analysis of nonlinear flows," *Journal of Fluid Mechanics*, vol. 641, pp. 115–127, 2009.

[64] M. Costa, A. L. Goldberger, and C.-K. Peng, "Broken asymmetry of the human heartbeat: loss of time irreversibility in aging and disease," *Physical Review Letters*, vol. 95, no. 19, p. 198102, 2005.

[65] M. Kurt, H. Chen, Y. S. Lee, D. M. McFarland, L. A. Bergman, and A. F. Vakakis, "Nonlinear system identification of the dynamics of a

vibro-impact beam: Numerical results," *Archive of Applied Mechanics*, vol. 82, no. 10-11, pp. 1461–1479, 2012.

[66] M. Grilli, A. Vázquez-Quesada, and M. Ellero, "Transition to turbulence and mixing in a viscoelastic fluid flowing inside a channel with a periodic array of cylindrical obstacles," *Physical Review Letters*, vol. 110, no. 17, p. 174501, 2013.

[67] M. Grilli, P. J. Schmid, S. Hickel, and N. A. Adams, "Analysis of unsteady behaviour in shockwave turbulent boundary layer interaction," *Journal of Fluid Mechanics*, vol. 700, pp. 16–28, 2012.

[68] M. F. Fathi, A. Bakhshinejad, A. Baghaie, and R. M. DSouza, "Dynamic denoising and gappy data reconstruction based on dynamic mode decomposition and discrete cosine transform," *Applied Sciences*, vol. 8, no. 9, p. 1515, 2018.

[69] S. S. Gopalakrishnan, B. Pier, and A. Biesheuvel, "Dynamics of pulsatile flow through model abdominal aortic aneurysms," *Journal of Fluid Mechanics*, vol. 758, pp. 150–179, 2014.

[70] O. San and A. E. Staples, "Dynamics of pulsatile flows through elastic microtubes," *International Journal of Applied Mechanics*, vol. 4, no. 01, p. 1250006, 2012.

[71] J. R. Womersley, "XXIV. oscillatory motion of a viscous liquid in a thin-walled elastic tubeI: The linear approximation for long waves," *The London, Edinburgh, and Dublin Philosophical Magazine and Journal of Science*, vol. 46, no. 373, pp. 199–221, 1955.

[72] M. Zamir and E. Ritman, *The physics of pulsatile flow*. Springer, 2000.

[73] A. Shamloo, M. A. Nejad, and M. Saeedi, "Fluid-structure interaction simulation of a cerebral aneurysm: Effects of endovascular coiling treatment and aneurysm wall thickening," *Journal of the Mechanical Behavior of Biomedical Materials*, vol. 74, pp. 72–83, 2017.

[74] H. J. Steiger, R. Aaslid, S. Keller, and H.-J. Reulen, "Strength, elasticity and viscoelastic properties of cerebral aneurysms," *Heart and Vessels*, vol. 5, no. 1, pp. 41–46, 1989.

[75] N. Koshiba, J. Ando, X. Chen, and T. Hisada, "Multiphysics simulation of blood flow and ldl transport in a porohyperelastic arterial wall model," *Journal of Biomechanical Engineering*, vol. 129, no. 3, pp. 374–385, 2007.

[76] G. G. Ferguson, "Direct measurement of mean and pulsatile blood pressure at operation in human intracranial saccular aneurysms," *Journal of Neurosurgery*, vol. 36, no. 5, pp. 560–563, 1972.

[77] A. Shah and J. Humphrey, "Finite strain elastodynamics of intracranial saccular aneurysms," *Journal of Biomechanics*, vol. 32, no. 6, pp. 593–599, 1999.

[78] D. Aranda-Iglesias, C. Ramón-Lozano, and J. Rodríguez-Martínez, "Nonlinear resonances of an idealized saccular aneurysm," *International Journal of Engineering Science*, vol. 121, pp. 154–166, 2017.

[79] P. A. Yushkevich, J. Piven, H. Cody Hazlett, R. Gimpel Smith, S. Ho, J. C. Gee, and G. Gerig, "User-guided 3D active contour segmentation of anatomical structures: Significantly improved efficiency and reliability," *Neuroimage*, vol. 31, no. 3, pp. 1116–1128, 2006.

[80] D. H. Spodick, P. Raju, R. L. Bishop, and R. D. Rifkin, "Operational definition of normal sinus heart rate," *The American journal of cardiology*, vol. 69, no. 14, pp. 1245–1246, 1992.

[81] M. Modat, G. R. Ridgway, Z. A. Taylor, M. Lehmann, J. Barnes, D. J. Hawkes, N. C. Fox, and S. Ourselin, "Fast free-form deformation using graphics processing units," *Computer Methods and Programs in Biomedicine*, vol. 98, no. 3, pp. 278–284, 2010.

[82] D. Rueckert, L. I. Sonoda, C. Hayes, D. L. Hill, M. O. Leach, and D. J. Hawkes, "Nonrigid registration using free-form deformations: application to breast mr images," *IEEE transactions on medical imaging*, vol. 18, no. 8, pp. 712–721, 1999.

[83] K. K. Chen, J. H. Tu, and C. W. Rowley, "Variants of dynamic mode decomposition: Boundary condition, Koopman, and Fourier analyses," *Journal of Nonlinear Science*, vol. 22, no. 6, pp. 887–915, 2012.

[84] R. Muthupillai, D. Lomas, P. Rossman, J. F. Greenleaf, A. Manduca, and R. L. Ehman, "Magnetic resonance elastography by direct visualization of propagating acoustic strain waves," *Science*, vol. 269, no. 5232, pp. 1854–1857, 1995.

[85] S. A. Kruse, G. H. Rose, K. J. Glaser, A. Manduca, J. P. Felmlee, C. R. Jack Jr, and R. L. Ehman, "Magnetic resonance elastography of the brain," *Neuroimage*, vol. 39, no. 1, pp. 231–237, 2008.

[86] M. Kurt, L. Wu, K. Laksari, E. Ozkaya, Z. M. Suar, H. Lv, K. Epperson, K. Epperson, A. M. Sawyer, D. Camarillo *et al.*, "Optimization of a multifrequency magnetic resonance elastography protocol for the human brain," *Journal of Neuroimaging*, 2019.

[87] E. Nikolova, I. Jordanov, Z. Dimitrova, and N. Vitanov, "Evolution of nonlinear waves in a blood-filled artery with an aneurysm," in *AIP Conference Proceedings*, vol. 1895, no. 1. AIP Publishing, 2017, p. 070002.

[88] H. W. Haslach and J. D. Humphrey, "Dynamics of biological soft tissue and rubber: Internally pressurized spherical membranes surrounded by a fluid," *International Journal of Non-Linear Mechanics*, vol. 39, no. 3, pp. 399–420, 2004.

[89] M. Hayakawa, K. Katada, H. Anno, S. Imizu, J. Hayashi, K. Irie, M. Negoro, Y. Kato, T. Kanno, and H. Sano, "CT angiography with electrocardiographically gated reconstruction for visualizing pulsation of intracranial aneurysms: identification of aneurysmal protuberance presumably associated with wall thinning," *American Journal of Neuroradiology*, vol. 26, no. 6, pp. 1366–1369, 2005.

[90] E. Oubel, J. Cebral, M. De Craene, R. Blanc, J. Blasco, J. Macho, C. Putman, and A. Frangi, "Wall motion estimation in intracranial aneurysms," *Physiological Measurement*, vol. 31, no. 9, p. 1119, 2010.

[91] K. Jain, S. Roller, and K.-A. Mardal, "Transitional flow in intracranial aneurysms–a space and time refinement study below the kolmogorov scales using lattice boltzmann method," *Computers & Fluids*, vol. 127, pp. 36–46, 2016.

[92] T. Aoki, K. Yamamoto, M. Fukuda, Y. Shimogonya, S. Fukuda, and S. Narumiya, "Sustained expression of mcp-1 by low wall shear stress loading concomitant with turbulent flow on endothelial cells of intracranial aneurysm," *Acta neuropathologica communications*, vol. 4, no. 1, p. 48, 2016.

[93] J. Xiang, V. Tutino, K. Snyder, and H. Meng, "Cfd: computational fluid dynamics or confounding factor dissemination? the role of hemodynamics in intracranial aneurysm rupture risk assessment," *American Journal of Neuroradiology*, vol. 35, no. 10, pp. 1849–1857, 2014.

[94] M. D. Ford and U. Piomelli, "Exploring high frequency temporal fluctuations in the terminal aneurysm of the basilar bifurcation," *Journal of biomechanical engineering*, vol. 134, no. 9, 2012.

[95] D. M. Sforza, C. M. Putman, and J. R. Cebral, "Hemodynamics of cerebral aneurysms," *Annual Review of Fluid Mechanics*, vol. 41, pp. 91–107, 2009.